AIP Physics of Plasmas

The Madison plasma dynamo experiment: A facility for studying laboratory plasma astrophysics

C. M. Cooper, J. Wallace, M. Brookhart, M. Clark, C. Collins, W. X. Ding, K. Flanagan, I. Khalzov, Y. Li, J. Milhone, M. Nornberg, P. Nonn, D. Weisberg, D. G. Whyte, E. Zweibel, and C. B. Forest

Citation: Physics of Plasmas (1994-present) **21**, 013505 (2014); doi: 10.1063/1.4861609
View online: http://dx.doi.org/10.1063/1.4861609
View Table of Contents: http://scitation.aip.org/content/aip/journal/pop/21/1?ver=pdfcov
Published by the AIP Publishing

PHYSICS OF PLASMAS **21**, 013505 (2014)

The Madison plasma dynamo experiment: A facility for studying laboratory plasma astrophysics

C. M. Cooper,[1,2] J. Wallace,[1] M. Brookhart,[1,2] M. Clark,[1] C. Collins,[1,2] W. X. Ding,[3] K. Flanagan,[1] I. Khalzov,[1,2] Y. Li,[1] J. Milhone,[1,2] M. Nornberg,[1,2] P. Nonn,[1] D. Weisberg,[1,2] D. G. Whyte,[4] E. Zweibel,[1,2,5] and C. B. Forest[1,2]
[1]*Department of Physics, University of Wisconsin, Madison, Wisconsin 53706, USA*
[2]*Center for Magnetic Self Organization, University of Wisconsin, Madison, Wisconsin 53706, USA*
[3]*Department of Physics and Astronomy, University of California, Los Angeles, Los Angeles, California 90024, USA*
[4]*Plasma Science and Fusion Center, Massachusetts Institute of Technology, Cambridge, Massachusetts 02139, USA*
[5]*Department of Astronomy, University of Wisconsin, Madison, Wisconsin 53706, USA*

(Received 8 October 2013; accepted 19 December 2013; published online 14 January 2014)

The Madison plasma dynamo experiment (MPDX) is a novel, versatile, basic plasma research device designed to investigate flow driven magnetohydrodynamic instabilities and other high-β phenomena with astrophysically relevant parameters. A 3 m diameter vacuum vessel is lined with 36 rings of alternately oriented 4000 G samarium cobalt magnets, which create an axisymmetric multicusp that contains $\sim$14 m^3 of nearly magnetic field free plasma that is well confined and highly ionized (>50%). At present, 8 lanthanum hexaboride ($\mathrm{LaB_6}$) cathodes and 10 molybdenum anodes are inserted into the vessel and biased up to 500 V, drawing 40 A each cathode, ionizing a low pressure Ar or He fill gas and heating it. Up to 100 kW of electron cyclotron heating power is planned for additional electron heating. The $\mathrm{LaB_6}$ cathodes are positioned in the magnetized edge to drive toroidal rotation through $\mathbf{J} \times \mathbf{B}$ torques that propagate into the unmagnetized core plasma. Dynamo studies on MPDX require a high magnetic Reynolds number $Rm > 1000$, and an adjustable fluid Reynolds number $10 < Re < 1000$, in the regime where the kinetic energy of the flow exceeds the magnetic energy ($M_A^2 = (\mathrm{v}/\mathrm{v}_A)^2 > 1$). Initial results from MPDX are presented along with a 0-dimensional power and particle balance model to predict the viscosity and resistivity to achieve dynamo action. © *2014 AIP Publishing LLC*. [http://dx.doi.org/10.1063/1.4861609]

I. INTRODUCTION

The Madison plasma dynamo experiment (MPDX) is designed to create a steady-state, hot, weakly magnetized, flowing plasma in which the kinetic energy of the flow drives magnetohydrodynamic (MHD) instabilities. Such a device accesses a new regime relevant to astrophysical applications and never before achieved in a laboratory.[1] This plasma is well-suited for studying astrophysical phenomena such as the dynamo process,[2] the feasibility of which is the topic of several recent publications[3–5] and is investigated in Sec. IV A. The magneto-rotational instability (MRI)[6] could also be investigated using the tunable boundary driven flow or a supplemental central spinning post in conjunction with an external Helmholtz coil. In addition, many basic plasma physics experiments studying interactions and organization of flows and magnetic fields can be performed.

Previous and ongoing dynamo experiments[7] use flowing liquid metals, which can be stirred mechanically and confined with a simple vessel. These interesting experiments suffer from several limitations, which can be avoided by using plasmas. First, the magnetic Reynolds number achieved in liquid metal experiments, which governs the transition to a dynamo, is too low. The magnetic Reynolds number $Rm = \mathrm{v}L/\eta$ (where L is the characteristic size, η is the resistivity, and v is the flow velocity) is the ratio of magnetic field advection by the flow to magnetic field diffusion from the resistivity. In liquid metal experiments, Rm is typically less than Rm_{crit} necessary for dynamo and MRI excitation. In addition, the fluid Reynolds number, which is the ratio of the momentum advection by the flow to the momentum diffusion by the viscosity $Re = \mathrm{v}L/\nu$ (where ν is the viscosity), cannot be varied independently of Rm in liquid metals. The ratio of these quantities, the magnetic Prandtl number $Pm = Rm/Re = \nu/\eta$ is a fixed, very small value $\sim 10^{-5}$ in liquid metal; thus, the flows required to exceed Rm_{crit} are always turbulent. In plasmas, by contrast, Rm can be varied independently of Re by controlling the plasma resistivity and viscosity by changing the electron temperature, the plasma density, and the ion species. $Pm \sim 1$ is achievable in MPDX making these plasmas excellent candidates for dynamo action and comparison to simulations. In addition, laminar dynamo action ($Rm > Rm_{crit}$, $Re < \sim 1000$) can be studied in the absence of fluid turbulence, which can suppress it.[8]

To experimentally test theories about the dynamo mechanism in a plasma, the device operates in the *flow-dominated* regime as opposed to the *magnetically dominated* regime. Such an experiment requires not only that Rm be large but also that the flow energy dominates over the magnetic energy. This is quantified by the Alfvén Mach number squared $M_A^2 = (\mathrm{v}/\mathrm{v}_A)^2$, which is the ratio of the inertial force to the magnetic force, where $\mathrm{v}_A = B/\sqrt{\mu_o n_i m_i}$ is the Alfvén velocity. When $M_A \gg 1$ and $Rm \gg 1$, flows can stretch and amplify the magnetic field. The feasibility of creating such a plasma in the lab has recently been demonstrated in a novel multi cusp confined plasma with electrostatic stirring,[9] where unmagnetized plasmas with flows of ~10 km/s have been created.[10] For MPDX class plasmas, a convenient set of formulae are

$$Re = 7.8\, \mathrm{v}_{\mathrm{km/s}} L_m n_{i,10^{18}\mathrm{m}^{-3}} Z^4 \sqrt{\mu}/T_{i,\mathrm{eV}}^{5/2}, \tag{1}$$

$$Rm = 1.6\, T_{e,\mathrm{eV}}^{3/2} \mathrm{v}_{\mathrm{km/s}} L_m/Z, \tag{2}$$

$$M_A = 0.46\, \mathrm{v}_{\mathrm{km/s}} \sqrt{\mu n_{i,10^{18}\mathrm{m}^{-3}}}/B_g, \tag{3}$$

where the Braginskii viscosity and the Spitzer resistivity for unmagnetized plasma are used for ν and η, respectively, $n_{i,10^{18}}$ is the ion density in $10^{18}/\mathrm{m}^3$, μ is the atomic mass in amu, Z is the net charge of the ions, $T_{e,\mathrm{eV}}$ and $T_{i,\mathrm{eV}}$ are the electron and ion temperatures, respectively, in eV, L_m is the characteristic size in meters, $\mathrm{v}_{\mathrm{km/s}}$ is the plasma velocity in units of km/s and B_g is a characteristic strength of the background magnetic field in Gauss. The plasma parameters and relevant dimensionless parameters are adjusted by controlling the neutral fill pressure, input power, gas species, and torques imposed on the plasma edge.

The MPDX uses several well-established techniques to confine and stir a hot, unmagnetized plasma. First, an axisymmetric multipole magnetic ring cusp built from alternating rings of individual permanent magnets creates a strong magnetic field localized to the edge, forming a magnetic bucket to confine the plasma. Second, biased hot cathodes draw current to induce an $\mathbf{J} \times \mathbf{B}$ rotation to stir the edge of the plasma. The flow is driven at the boundary and momentum is viscously transported throughout the unmagnetized region. By controlling the spatial profile of these boundary-driven flows, arbitrary large scale helical flows can be established (Fig. 1).

The paper is organized as follows: Section II provides a description of the device, its construction and initial operation. Section II C describes the LaB$_6$ cathodes, which are used for producing plasma and controlling the boundary flow. Section II D describes the current state of diagnostics on MPDX. Section III presents initial measurements of plasma parameters in the MPDX operation that provides the basis for scaling to higher power. Section IV outlines simulations predicting machine confinement and operation as well as providing a plan for achieving several types of dynamo action in MPDX.

II. DESCRIPTION OF THE MPDX

New parameter regimes in laboratory plasmas can be reached due to recent breakthroughs in plasma physics technologies. This section describes the design of the facility, vacuum chamber, magnets, and plasma sources.

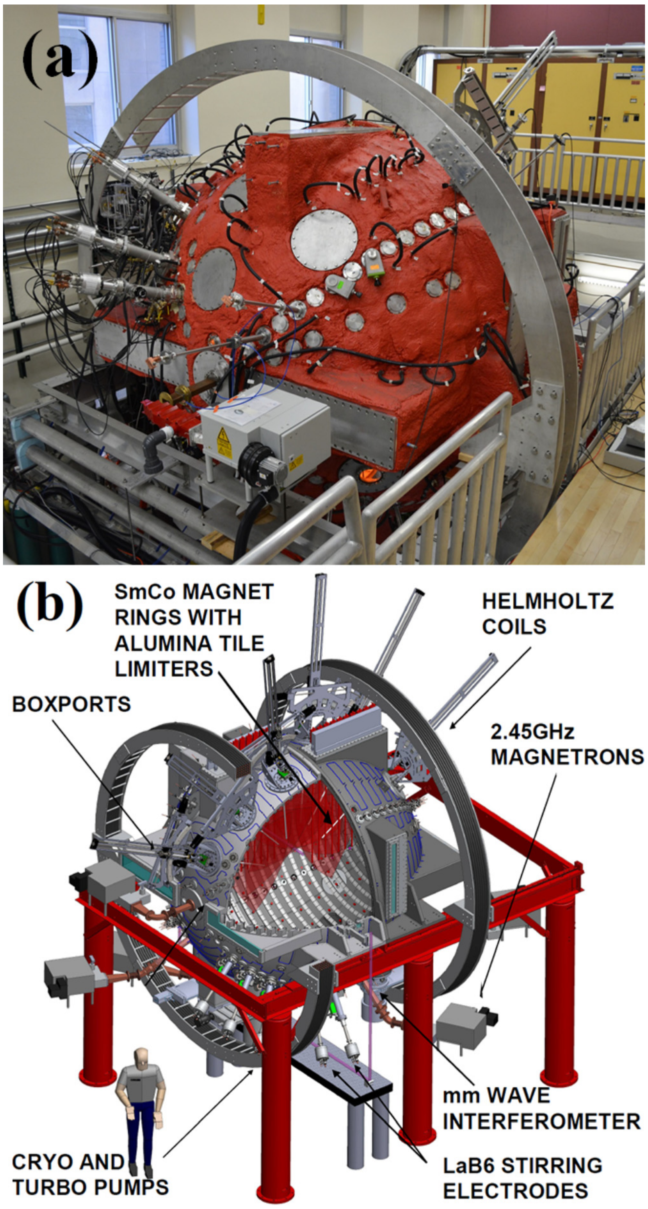

FIG. 1. (a) A picture of MPDX and (b) the various current and planned subsystems labeled.

A. Vacuum chamber

The experimental vacuum chamber is comprised of two 3 m diameter hemispherical shells joined by equatorial flanges to create a spherical vessel. One hemisphere is mounted on a linear stage to provide easy opening and access to the chamber interior. The hemispherical shells are made of 0.03 m thick cast A356 aluminum (see Fig. 2). The wall thickness is determined by structural integrity and the need to provide sufficient material to machine flanges and other features into the walls.

Each hemisphere is cast as a single piece by Portage Casting and Molding, Inc., which provides many benefits over a traditional welded vacuum vessel. Casting not only eliminates the need for costly vacuum welds but also has allowed for a more complex and precise design at a greatly reduced cost. The design process resembled "3D Printing:" Solidworks[11] computer aided design software was used by

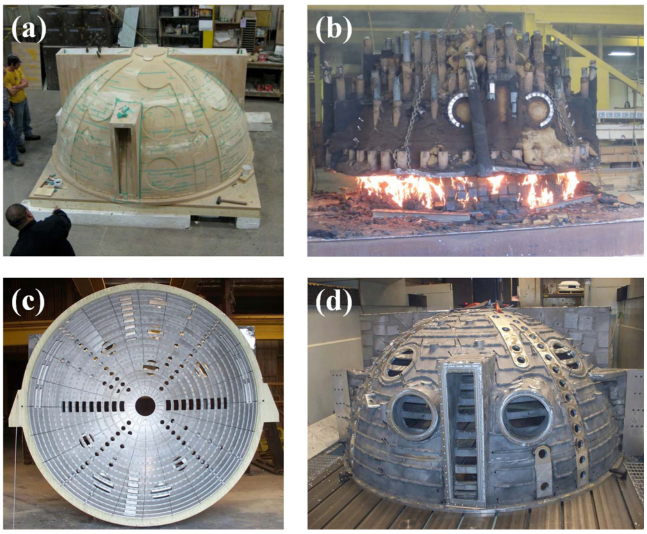

FIG. 2. (a) The positive of the chamber used to make the mold. (b) The casting process for the vessel in the mold. (c) The fully machined interior of one hemisphere of the vacuum vessel. Precision located rings with planar facets and tapped holes for each magnet provide for the cusp field. (d) The exterior of the vacuum vessel showing ports, magnet bridging, and embedded vessel cooling.

the UW engineering team to design the machine. The design was sent to the aluminum casting firm, where a 5 axis milling machine was used to construct a positive (i.e., pattern) for the mold. Sand molds were made, and molten aluminum was cast into the molds. Stainless steel tubular cooling lines are cast directly into the walls providing a low thermal impedance to remove heat from the experiment. Fig. 2 shows the construction.

The vessel features six identical boxports (0.2 m $\times$ 1.0 m) on each hemisphere to provide large views for optical diagnostics. Each hemisphere has seven larger 0.35 m circular ports for probes and Radio-Frequency (RF) heating sources. Each pole has a 0.35 m port for RF feedthroughs and to provide axial access. An additional 182 ports of 0.075 m are located on the sphere between magnet rings for insertion of plasma stirring electrodes, diagnostics, or electrical connections. The chamber interior is plasma spray coated with a 0.00025 m thick alumina film. The large diameter seals (including the seals between the two hemispheres) are differentially pumped double O-ring seals. Two 2000 l/m turbo pumps and two 4000 l/m cryo pumps routinely achieve 5×10^{-7} Torr vacuum base pressure, similar to stainless steel vessels sealed with O-rings. The experimental operating pressure with gas fill is $<5 \times 10^{-4}$ Torr.

B. Magnets

Eighteen faceted rings are precisely machined into each hemisphere interior and used for mounting the ~3000 0.038 m $\times$ 0.025 m $\times$ 0.05 m samarium cobalt (SmCo) magnets. Unlike neodymium (NdFeB) magnets, SmCo magnets do not corrode in the presence of hydrogen gas. Each ring of magnets alternates in polarity, creating a 36 pole, axisymmetric magnetic field cusp for plasma confinement. The magnets are in good thermal contact with the water cooled vacuum vessel and operate at temperatures up to 40 °C, far below their curie temperature of 350 °C. The magnets are covered by Kapton film and thin interlocking alumina ceramic tiles that protect and electrically isolate them.

The primary role of the magnets is to confine the large unmagnetized spherical volume of plasma for basic plasma experiments. The result from a Maxwell SV finite element modeling of the magnetic field used to design the magnet geometry is shown in Fig. 3. The magnetic field is <1 G 0.25 m away from the magnet face. Residue marks on the tiles appeared after 10 h of integrated "plasma on" time and indicate the footprint of the plasma contact with the tiles. They are 0.0008 m wide, in good agreement with the width predicted by theory for our plasma parameters.[12] The magnet ring spacing in the MPDX is 0.11 m, which implies that loss area is less than 1% of the surface area of the vessel. The MPDX confines ~14 m^3 of plasma with a convective plasma loss surface area of ~0.2 m^2. Particle and energy confinement pertaining to achievable parameters in MPDX are further investigated in Sec. IV.

The cusp field also plays an important role in providing a surface for a 2.45 GHz electron-cyclotron resonance (where $B = 875$ G, approximately 0.05 m in front of the magnets as seen in Fig. 3). Five magnetrons manufactured by CoberMuegge, LLC, are being installed to provide up to 100 kW continuous power for ionizing and heating the plasma. Simple unterminated waveguide is used for antennas in either O-mode or X-mode polarization relative to the direction of the cusp magnetic field. Such sources are routinely used for heating overdense plasmas (n_e greater than the critical density $7 \times 10^{16}\ \mathrm{m}^{-3}$ for 2.45 GHz). This is speculated to be either be due to mode conversion to the electron Bernstein wave or by parallel propagation from the high field side of R-waves (whistler waves), neither of which suffers from the cutoff. Additionally, the magnetic fields are necessary for generating flows in conjunction with the LaB_6 cathodes and molybdenum anodes.

An external Helmholtz coil is now being installed for introducing a seed magnetic field and to probe the interactions between the driven flows and a scalable background magnetic field.

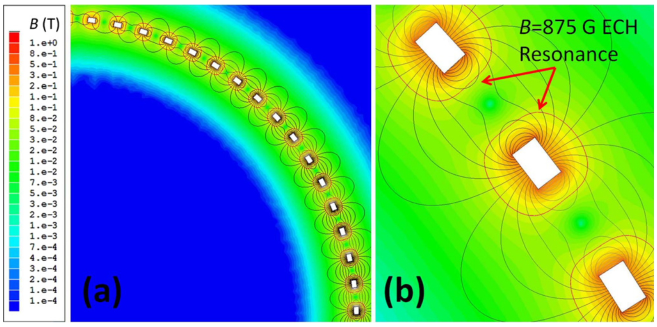

FIG. 3. (a) Poloidal magnetic flux contours for the MPDX (magnetic field lines) and color contours of the magnetic field strength as computed by the Maxwell SV finite element modeling package and (b) a closeup of the cusp. The magnetic field is generated by axisymmetric rows of 4000 G SmCo magnets with alternating polarity. The central dark blue contour shows the region where the magnet-produced field is less than 0.2 G and the red contour shows the 875 G ECH resonance surface.

C. LaB$_6$ stirring electrodes

Lanthanum Hexaboride has long been used as a high temperature ($T_e < 30\,\text{eV}$), high density ($n_e < 2 \times 10^{19}\,\text{m}^{-3}$) plasma source due to its high input power density and robust construction.[13–16] The ability to stir the MPDX plasma through LaB$_6$ cusp biasing is possible because LaB$_6$ can withstand high bias voltages ($V_d < 500\,\text{V}$).

The LaB$_6$ stirring electrode design developed for MPDX is shown in Fig. 4. The cylindrical LaB$_6$ cathode (measuring 0.056 m in length, 0.0264 m in diameter, with 0.003 m thick walls) is radiatively heated up to 1600 °C by an internal graphite heater filament. This filament is precision machined with a five-fluted current path and threaded ends to ensure tight electrical connections. To prevent arcing, the heater filament is electrically isolated from the AC heater power supply with an isolation transformer and does not touch the LaB$_6$ cathode. A stainless steel tube allows for a sliding vacuum seal, a press-fitted plastic bushing provides structural support for the 12 kg electrode, and a large stainless steel "garage" allows the cathode to be completely retracted behind a gate-valve for periodic maintenance. The conductors for the heater circuit as well as the cathode discharge circuit are cylindrical copper tubes with a center molybdenum rod, coaxially nested inside the stainless steel tube and isolated from each other and the surrounding plasma by quartz tubing.

In anticipation of the large amounts of RF power provided by MPDX's magnetrons, the three electrical feedthroughs per electrode are each paired with a copper clamp that fulfills three essential functions: electrical connection to power supply cables, water cooling to the cylindrical conductor bases, and transmission line choking of RF waves.

Each LaB$_6$ stirring electrode is paired with one or more molybdenum anodes poloidally displaced one cusp. The current path between cathode and anode must cross a permanent magnet ring and produces $\mathbf{J} \times \mathbf{B}$ torque in the toroidal direction, as shown in Fig. 5. Azimuthal particle drifts rapidly symmetrize the potential,[10] creating a virtual cathode connected to the actual cathode, but toroidally symmetric. This edge-applied torque couples to the bulk plasma via ion-ion viscosity. Initial experiments using these electrodes have injected up to 40 A of current at 500 V. Each anode-cathode potential will eventually be independently set, creating a customizable poloidal profile of toroidal velocity.

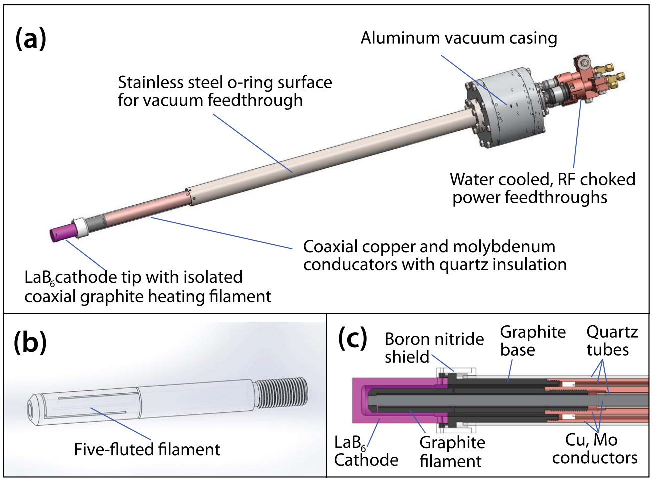

FIG. 4. LaB$_6$ stirring electrode design. The entire (1.1 m long) electrode is shown in (a), with detailed views of (b) the graphite heater filament and (c) the LaB$_6$ tip. Not shown: the linear vacuum feedthrough and garage/gate-valve assembly.

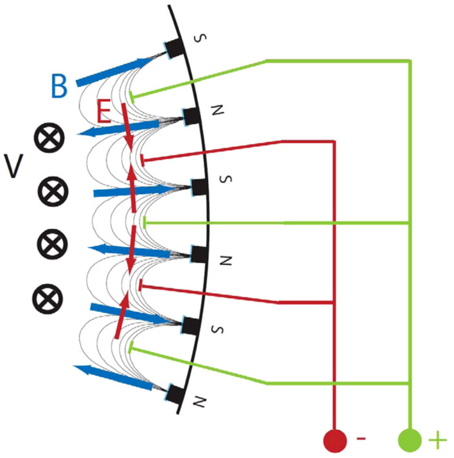

FIG. 5. A cartoon of the flow drive mechanism in MPDX using biased anode-cathode pairs in the cusp field. The torque is proportional to the anode-cathode bias voltage, current, and their location in the cusp, which determines B.

D. Diagnostics

The MPDX plasma is diagnosed by physical probes capable of making *in situ* measurements of local plasma parameters. These probes can all be pumped down and inserted into the machine via vacuum gate valves without interrupting operation. The plasma temperature and density are low enough for long probe lifetimes. The surface area of the probes and probe shafts is much smaller than the loss area on the cusp, and individual probes do not perturb the plasma.

A swept voltage bias is applied to the tip of planar Langmuir probes to create an "I-V" curve. This curve is analyzed to determine T_e, n_e, Φ_p, and Φ_f using standard Langmuir probe techniques.[17] Plasma flows inside MPDX are measured using Mach probes. The probe tips are biased several times T_e below the plasma potential to collect ion saturation current and the Mach number and absolute speed can be measured using standard techniques.[17] A triple probe is used to provide an additional measurement of T_e and Φ_f.

A phase locked set of 1 mm sources acquired from Virginia Diodes, along with two mixers and an Analog Devices phase detector provide a single channel interferometric measurement of the line-integral density. The 1 mm wavelength is optimal for normal MPDX densities of $\sim 10^{17}$–$10^{18}\,\text{m}^{-3}$ when integrated along a 6 m pathlength twice the length of the MPDX plasma. These densities correspond to phase shifts from $\sim \frac{\pi}{2}$ to 4π, which are easily measurable. The upper bound for a measurable density is $n_e \sim 10^{21}\,\text{m}^{-3}$ and the minimum detectable density set by the digitizer noise levels is $\sim 10^{15}\,\text{m}^{-3}$, a sufficient resolution for MPDX densities. An example calibrated interferometer time trace is found in Fig. 6.

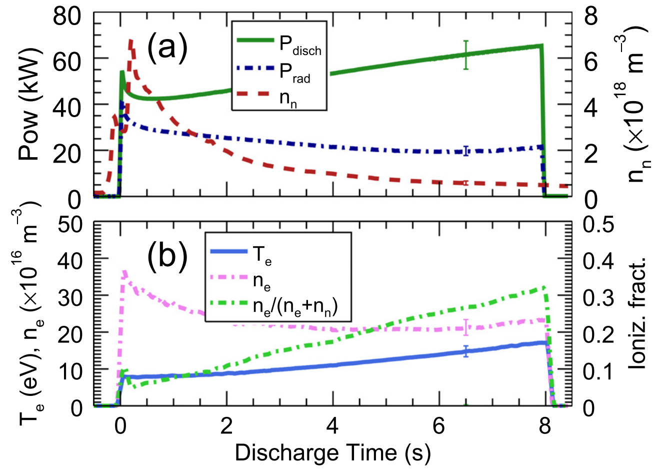

FIG. 6. (a) Time trace of the gas puff, the input power, and the radiated power from the bolometer (b) T_e measured by a Langmuir probe, n_e measured by an interferometer normalized to a path length measured by probes, and the calculated ionization fraction $n_e/(n_n + n_e)$.

A bolometer made from a LiTa crystal is installed on the MPDX to measure the total radiated power. This includes light radiated from the neutral particles and ions due to collisions with electrons, as well as the incident kinetic energy of any superthermal neutral gas created through elastic and charge exchange collisions. The only power loss rate not included is the ionization power losses and the losses to the wall. The bolometer is calibrated with a laser over a scaling of incident power.

Magnetic diagnostics consist of an array of Hall probes mounted on the MPDX surface to measure the multipole moment of the slowly varying magnetic fields. Rogowski coils on probes inside the plasma will be calibrated and integrated[18] to measure the weak, fluctuating magnetic fields.

A two dimensional movable probe drive is mounted on the MDPX vessel with a gate valve and a rotatable vacuum ball valve. Two stepper motors mounted perpendicular to each other can change the position of the probe inside the machine, allowing the probe to trace out a plane of data as seen in Fig. 7. The probe drive can be used with many types of probes in MPDX and is very important for studying 2D systems in MPDX.

The data collected by the diagnostics are digitized by a 500 kHz 96-channel ACQ-196 module from D-TACQ Solutions Ltd, recorded by a computer and stored for analysis. Information about the MPDX such as the machine conditions, average plasma parameters, and probe positions are recorded in a searchable SQL database. Probe movement and discharge parameters are controlled by a Labview interface via a Compact RIO. The machine can be run in a pulsed operation or in a steady-state mode. The MPDX has created over 3000 discharges and nearly 3 h of "plasma on" time total. Plasma discharges are fully automated and create 3-5 s plasma discharges every 45 s around the clock.

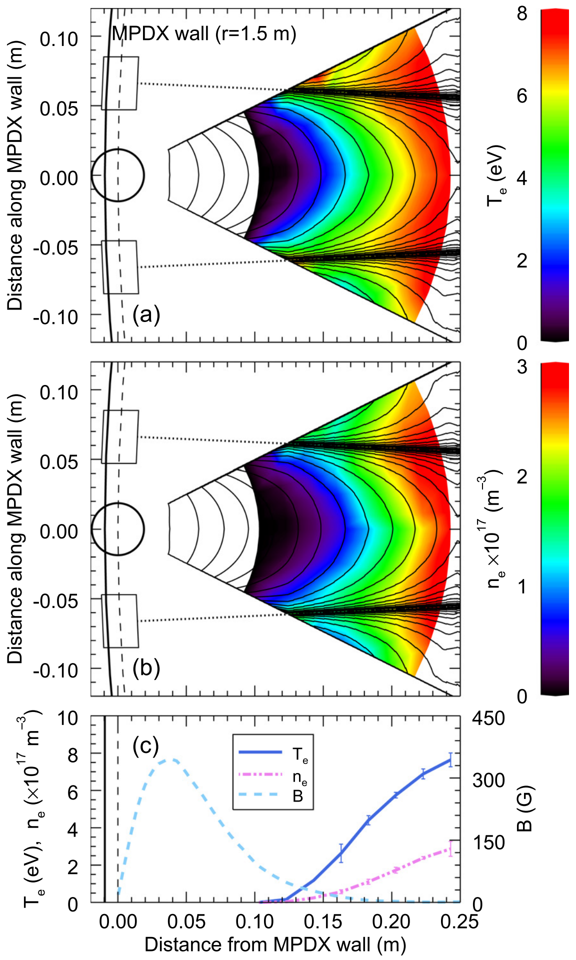

FIG. 7. 2D plasma profiles of (a) T_e and (b) n_e for a 45 kW discharge in a gas puff corresponding to when $n_n = 1\times10^{18}\,\mathrm{m}^{-3}$ helium. Isopotentials of the magnetic potential $\log(\Psi)$ found from integrating the measured cusp field are plotted over the data. A radial cut of the data along the center of the plane is shown in (c) along with the measured value of the magnetic field. In the unmagnetized core of MPDX, $\beta = 100$ for $B = 1$ G and $Pm = 8$ for $T_i = 1$ eV. For $v_\phi = 5$ km/s, Re = 35, Rm = 270 in the MPDX core.

III. INITIAL MPDX RESULTS

The first major result from MPDX is exhibiting confinement of an unmagnetized plasma using the edge localized magnetic multipole cusp. Eight LaB_6 cathodes ($\theta = 30°, 40°, 50°, 60°, 125°, 135°, 145°, 155°$, $\phi = 225°$) and eight anodes, displaced one cusp poloidally and 90° toroidally ($\theta = 35°, 45°, 55°, 65°, 120°, 130°, 140°, 150°$, $\phi = 135°$), were inserted radially into the unmagnetized region ($r = 1.25$ m). The cathodes were biased 200–500 V with respect to the anodes, with each cathode drawing 5–40 A for a discharge time of 3–10 s in order to characterize the breakdown and confinement in the MPDX. Electron heating was provided exclusively by the Ohmic heating of the anode-cathode circuit.

The machine can create steady state plasma discharges with a constant input power and fill pressure where plasma parameters stay constant over the length of the shot. However, the most interesting plasma regimes come where the neutral gas is puffed in, over a 20 ms time, 0.5 s before discharge, achieving a neutral fill pressure high enough to achieve breakdown that is then pumped out to achieve high ionization fractions and electron temperatures. An example time trace for an 8 s discharge at 400 V drawing a total of 150 A for a helium gas puff is shown in Fig. 6. A Langmuir probe was inserted radially into the unmagnetized region ($r = 1.12\,\text{m}$), $\theta = 110°, \phi = 45°$ and continuously swept $-80\,\text{V}$ to $+20\,\text{V}$ at 100 Hz to determine $T_e(t)$ in the core of MPDX. The interferometer was directed through a box port, reflected off the far wall and collected on the same side. The interferometer was normalized to the path length through the plasma as measured by probes to determine $n_e(t)$. The radiated power from the plasma from the bolometer was integrated over the surface area of the machine to yield the total radiated power for the experiment. The shot to shot reproducibility is comparable to the error in this measurement ($\delta T_e/T_e \sim 5\%$), which enables ensembled averaging of datasets over multiple shots and with the probe at different locations.

The neutral gas density decreases as the gas is pumped out over the course of the shot. With fewer neutral particles to ionize, the plasma density drops as well. With fewer losses to ionization, the walls, and collisions with the neutral gas and ions, the electrons heat up with the increase in input power. This is manifested in the ionization percentage, which increases from 5% to 35% over the course of the shot. However, this is the core n_e compared to n_n measured at the wall. In this plasma with $n_e \sim 2.5 \times 10^{17}\,\text{m}^{-3}$ and $T_e \sim 15\,\text{eV}$, the neutral mean free path for ionization in the reference frame of the neutral particle (the neutral penetration depth) is 0.75 m, meaning the center of the plasma (two e-foldings in radius) is nearly fully ionized. This will be investigated with passive spectroscopy. In addition, the radiated power measured by the bolometer drops even as the total input power rises. Using the below measured driven edge rotation speed of $\text{v}_\phi = 2.3\,\text{km/s}$ in a similar discharge yields a local $Rm = 320$, an important benchmark for studying the dynamo.

Two dimensional profiles of T_e and n_e of a helium plasma for a 45 kW discharge into a gas puff are shown in Fig. 7. The probe was moved in 2 cm radial steps and 6° toroidal steps over the 54° sampled (including 0°), creating an 8 point by 11 point plane. The swept Langmuir probe measured the steady state T_e at each position and the local n_e is determined from the measured ion saturation current, calibrated to the interferometer. A hall probe was used to measure the 3D magnetic field from the cusp on the same 2D plane as the plasma parameters at a 0.33 cm radial spacing and 3° toroidal spacing across the 54°. This magnetic field was integrated to yield the magnetic potential Ψ. Isopotentials of $\log(\Psi)$ are plotted over the data to elucidate how the field lines of the cusp contribute to confinement in MPDX by lowering the effective loss area at the wall, with $\Psi = 0$ on the line in the cusp perpendicular to the wall. The isopotentials are evenly spaced along a chord perpendicular to the wall, which indicates the predicted exponential drop-off in magnetic field. A 1D profile of the plasma along the 0° line is shown below with the measured magnetic field. No plasma can be measured between the cusps by the probe until it is 0.14 m from the wall ($r = 1.36\,\text{m}$), where B_{cusp} drops below 40 G. Prior measurements deeper into the plasma indicate that for $r < 1.32\,\text{m}$, T_e and n_e are relatively flat, indicating a homogeneous unmagnetized plasma core. In the core, $\beta = n_e k_B T_e \times 2\mu_o/B^2 \gg 1$, and unity Prandtl number is measured in the experiment, both important for studying the flow driven MHD instabilities.

The values of n_e and T_e characteristic of the unmagnetized core ($r = 1.12\,\text{m}$) were recorded for a scaling of input power 200–450 V, 20–300 A (4–135 kW) with a constant fill pressure 6.5×10^{-5} Torr of helium ($n_n = 2 \times 10^{18}\,\text{m}^{-3}$), as shown in Fig. 8. The ability to achieve a steady, chamber-filling breakdown with a discharge power as a low as 4 kW is also indicative of a well confined plasma. The electron temperature saturates at higher input power as the ionization cross section climbs non-linearly and incrementally hotter electrons are required for large changes in density. Higher T_e should be observed once the ionization percentage becomes sufficiently high. The total radiated power measured by the bolometer and integrated over the surface of MPDX is shown. Using the measured values of T_e, n_e, and the radiated power, a confinement model can be used to predict the equilibrium power as described in Sec. IV, plotted in the final panel. The experiment will eventually have up to 300 kW of heating power available.

The second major result is measuring the flow in MPDX. Only four cathodes and five anodes were used. The anodes and cathodes were retracted back into the magnetized edge cusp ($r = 1.40\,\text{m}$) at the same toroidal and poloidal locations described above. In this setup, the only closure path for current is across the cusp field resulting in a $\mathbf{J} \times \mathbf{B}$ torque in the toroidal direction. A two-sided Mach probe was inserted into the plasma oriented to measure the toroidal flow v_ϕ in the vicinity of the cathode $r = 1.35\,\text{m}$, $\theta = 55°, \phi = 45°$. An example time trace is shown in Fig. 9.

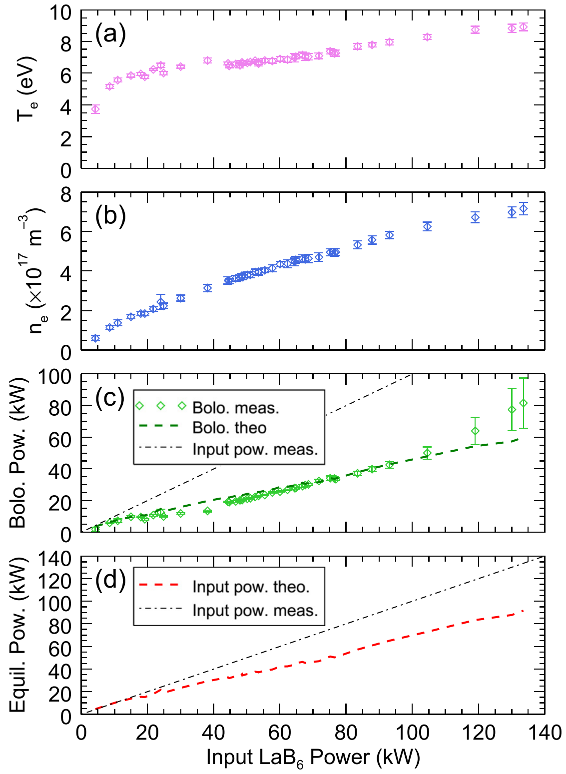

FIG. 8. The scaling of (a) T_e, (b) n_e, and (c) radiated power measured while varying the input power from 4 to 135 kW into 6.5×10^{-5} Torr helium. The data are used to predict the radiated and equilibrium power required using a confinement a model, which is compared to the input power (d) by the LaB_6 cathodes.

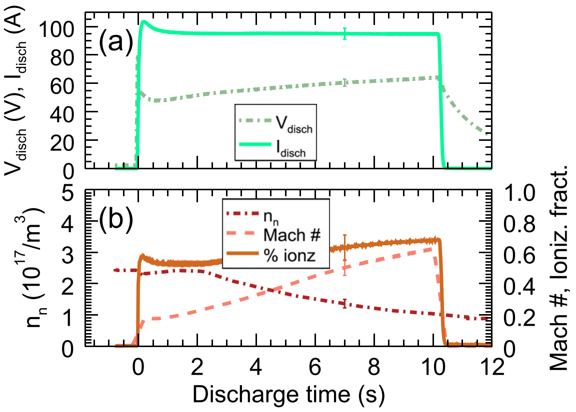

FIG. 9. (a) A time trace of the input voltage, current, and power as measured at the anode and cathode and (b) the toroidal flow v_ϕ measured by a Mach probe, the neutral density measured by a cold cathode gauge and the ionization percentage. As the puffed neutral gas is pumped out, the neutral drag decreases and the plasma spins faster.

To elucidate the flow, the neutral argon gas was puffed into the machine and pumped out over the course of the shot. In this moderately ionized regime, ion-neutral collisions which dissipate momentum can be comparable to ion-ion collisions which propagate momentum, and the density of the stationary neutral gas plays a role in regulating the flow. As the neutral density drops, the plasma-neutral gas drag lowers and the plasma rotation velocity for a given torque increases. In this shot, $T_e = 5.0\,\text{eV}$ and the plasma sound speed $c_s = 3.5\,\text{km/s}$, corresponding to a flow speed of $v_\phi = 2.3\,\text{km/s}$. Stirring unmagnetized plasmas with electrodes in a multicusp confinement scheme has been studied in detail in cylindrical device.[10]

IV. CONFINEMENT MODELING OF RESISTIVITY AND VISCOSITY

In the central unmagnetized region of the MPDX, transport rapidly eliminates any gradients in densities and temperatures allowing for a simple boundary model of plasma confinement. A zero-dimensional particle and power balance model is used to predict the plasma parameters (n_e, T_e) in the MPDX given a set of laboratory parameters (fill gas density and input power). The model includes both plasma physics and atomic physics to predict the particle and energy confinement time.

Volumetric neutral gas ionization by the plasma is balanced by plasma lost by convection to the wall through the magnetic cusps. Experiments and the best available theory suggested that cusp confinement limits plasma losses by effectively reducing the loss area of the boundary. The predicted magnetic cusp width $w_c = 4\sqrt{\rho_e \rho_i} \sim 0.0008\,\text{m}$ (Refs. 12 and 19) is proportional to the hybrid gyroradius, where $\rho_\alpha = v_{th,\alpha} m_\alpha c/eB$ is the gyroradius of a species α based on its thermal velocity $v_{th,\alpha}$, mass m_α. The total length of magnet faces $L_c = 220\,\text{m}$ in MPDX yielding a convective loss area $A_c = L_c \times w_c = 21 \times (T_e T_i \mu)^{1/4} B^{-1}\,\text{m}^2$ for the model, which depends on the magnitude of B at the surface of the magnet and weakly depends on T_e and T_i. There are additional losses to the cathodes, anodes, as well as any probes inserted into the plasma denoted as A_l.

The volumetric ionization rate $S_p = \langle \sigma_{iz} v_e \rangle n_n n_e$ for an ionization cross section σ_{iz} is balanced by a boundary flux $\Gamma_c = 0.5 n_e c_s$ such that $\int\int\int S_p\, dV = \int\int_{edge} \Gamma_c\, dA$. In the zero-dimensional limit, the volume integral can be replaced by the volume of the machine $\mathbb{V}$ and the surface integral can be replaced with $A_c + A_l$ yielding

$$\langle \sigma_{iz} v_e \rangle n_e n_n \mathbb{V} = 0.5 n_e c_s (A_c + A_l). \tag{4}$$

Equation (4) is transcendental in T_e and independent of n_e. It determines the neutral density n_n in the presence of the plasma in MPDX. This is related to the experimental fill density $n_f = n_e + n_n$.

The power balance in MPDX is similarly modeled by comparing the power added to the system by LaB$_6$ cathodes and magnetrons Q_{tot} (in kW) to the power lost by volumetric radiation, ionization, and surface particle convection to the walls. In the 0D limit, this becomes

$$Q_{tot} = (\gamma_t k_B T_e + E_{iz}) 0.5 n_e c_s (A_c + A_l) + Q_{rad} + Q_{\alpha n}. \tag{5}$$

The total radiation Q_{rad} arises from electron-neutral collisions $Q_{r,n} = R_{r,n}(T_e) n_e n_n \mathbb{V}$ and electron-ion collisions $Q_{r,i} = R_{r,n}(T_e) n_e n_i \mathbb{V}$. The radiation coefficients associated with these processes, $R_{r,n}(T_e)$ and $R_{r,i}(T_e)$, were calculated from atomic rates used in the KPRAD code.[20] The heat lost to the neutral gas $Q_{\alpha n}$ consists of electron neutral elastic collisions $Q_{en} = 3(m_e/m_i) n_e k_B (T_e - T_n) \nu_{en} \mathbb{V}$, ion neutral elastic collisions $Q_{in} = (3/2) n_e k_B (T_i - T_n) \nu_{in} \mathbb{V}$, and charge exchange $Q_{cx} = n_e k_B (T_i - T_n) \nu_{cx} \mathbb{V}$. These depend on the elastic neutral gas collision rate for a species α, $\nu_{\alpha n} = n_n \sigma_n \sqrt{k_B T_\alpha / m_\alpha}$ with $\sigma_n \sim 5 \times 10^{-19}\,\text{m}^2$.

The total heat convected to a surface is modeled by the thermal transmission coefficient,[21]

$$\gamma_t = \frac{2}{1-\delta_e} + \frac{2T_i}{ZT_e} - 0.5\ln\left[\left(\frac{2\pi m_e}{m_i}\right)\left(Z + \frac{T_i}{T_e}\right)\frac{1}{(1-\delta_e)^2}\right], \tag{6}$$

which depends on the secondary electron emission coefficient δ_e and is only weakly dependent on the species via the mass ratio. For $T_e < 20\,\text{eV}$, $\delta_e = 0$ and $\gamma_t = 5$–8.

A given T_e and n_e and T_i uniquely determine neutral fill pressure and input power subject to particle and power conservation. Equation (4) is iteratively solved to find n_n. Equation (5) is iteratively solved using T_e to calculate Q_{tot}. A more sophisticated model which self consistently calculates T_i based on the ion power balance from collisions and viscous heating, as well as modeling the input beam power as a population of non-Maxwellian electrons will be presented in a future publication. However, the current model provides a reasonable prediction over much of the parameter ranges sought.

The model is benchmarked against MPDX data for $Q_{tot} < 150\,\text{kW}$ in Fig. 8. The measured values of n_e and T_e are used to calculate the radiated power flux. This rate is compared to the measured bolometer reading to give an approximation for the additional loss area A_l. A value of $A_l = 0.25$ m^2 fits the bolometer data best, which closely matches the surface area of the anodes, cathodes, and several probes in the machine. Using this additional loss area, the corresponding values of the equilibrium input power were calculated using Eq. (5). The result is plotted as a dashed line in Fig. 8(d). At high power, a fraction of the discharge electron beam is lost directly to the wall before it is thermalized and accounts for the difference between the measured input power (the total beam power) and the predicted equilibrium input power (just the thermalized beam). This fraction (as high as 25%) matches predictions based on the thermalization rate and the loss rate for a 450 eV electron. This loss fraction must be taken into account when designing the machine to operate at 300 kW coupled to the plasma, and an actual input power from LaB$_6$ may be higher.

The individual power loss mechanisms in the transport model are elucidated in Fig. 10. The total power Q_{tot} is the sum of all the power losses and represents the equilibrium input power required to sustain a plasma with the corresponding plasma parameters n_e and T_e. The power losses are dominated by ion radiation $Q_{r,i}$ in argon due to the high number of emission lines. While the neutral radiation rate increases with T_e, the neutral density decreases from enhanced ionization and there is a net decrease in neutral radiation $Q_{r,n}$ with increasing T_e. The plasma confinement decreases with increasing T_e and the plasma ionization rate and ionization power Q_{iz} increase with increasing T_e. The plasma power convected to the wall through the cusp Q_c increases with the higher losses and the higher thermal heat coefficient γ_t. This model applies to singly ionized ions only. When argon doubly ionizes, the radiation rate increases and the model predicts Q_{tot} too low at high values of T_e. However, line radiation ceases for doubly ionized helium and Q_{tot} should be lower than the model predicts at high values of T_e.

The confinement model predictions are used to calculate Re and Rm plotted in Fig. 11 for $v_\phi = 10\,\mathrm{km/s}$ and $T_i = 1$ eV, reasonable for the high input power and high ionization fractions. These predictions address the ability to achieve different types of dynamo action across a scaling of Pm in MPDX. To generate this plot, the input power is fixed at 300 kW and the plasma density is varied by changing the neutral fill pressure. This creates a tradeoff between $Rm \propto T_e^{3/2}$ and $Re \propto n_e$.

The confinement model estimates when magnetic effects become important in MPDX by calculating the magnetic field required for various magnetic dimensionless parameter benchmarks (Fig. 12). The estimates assume $v_\phi = 10\,\mathrm{km/s}$ for the same 300 kW discharge described above. MPDX will be unmagnetized (i.e., a *flow-dominated* regime) when the Alfvén Mach number $M_A > 1$ and when $\beta > 1$. This is satisfied for $B < 10$ G.

The external Helmholtz coils can be adjusted from $1\,\mathrm{G} < B < 350\,\mathrm{G}$. The magnetic effects on the plasma during the transition to magnetically dominated regime, such as the effects on viscosity, can be studied. The MPDX can also be configured to probe magnetized plasma regimes relevant to laboratory plasma astrophysics. A Lundquist number $S > 5000$ is estimated in MPDX for $B > 100$ G. The Lundquist number is the ratio of the $\mathbf{J} \times \mathbf{B}$ torque to the resistive magnetic diffusion force $S = \mu_o L v_A / \eta = Rm/M_A$. The

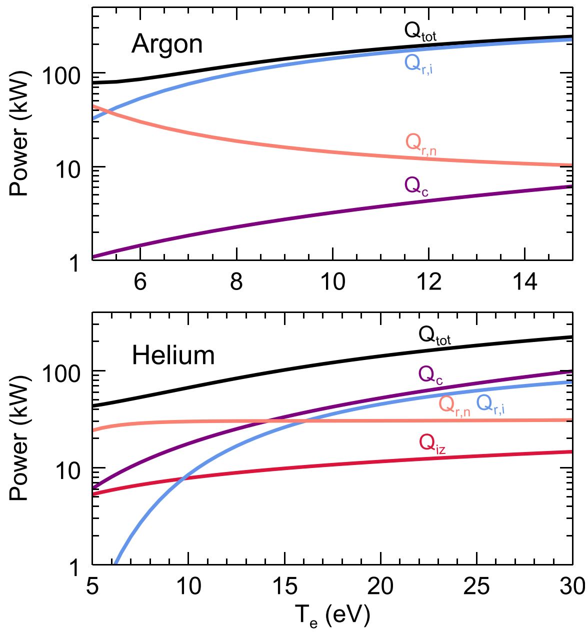

FIG. 10. The power balance calculated in the transport model in MPDX for argon ($n_e = 2 \times 10^{17}\,\mathrm{m}^{-3}$) and helium ($n_e = 5 \times 10^{17}\,\mathrm{m}^{-3}$) over a scaling of T_e. Q_{tot} is the total power in the experiment, Q_{iz} is the ionization power, Q_c is the convected flux to the wall through the sheath, $Q_{r,n}$ is the radiation from the neutral gas from electron-neutral collisions, $Q_{r,i}$ is the ion radiation from electron-ion collisions and dominates at high T_e. The thermal electron-ion and electron-neutral losses (<5 kW) are not shown. The maximum planned input power to MPDX is 300 kW.

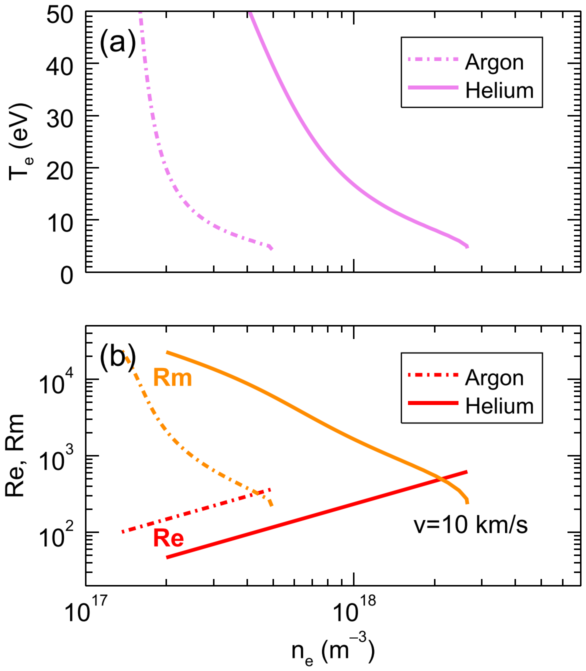

FIG. 11. Plasma parameters calculated using the confinement code described above for an input power of 300 kW and $v_\phi = 10\,\mathrm{km/s}$ over a scaling of n_e achieved by varying the fill pressure in argon (dashed) and helium (solid). (a) The tradeoff between T_e and n_e. (b) The tradeoff between Re (red) and Rm (orange). This creates a scaling of magnetic Prandtl number $0.01 < Pm = Rm/Re < 100$ with the intersections of the lines corresponding to $Pm = 1$.

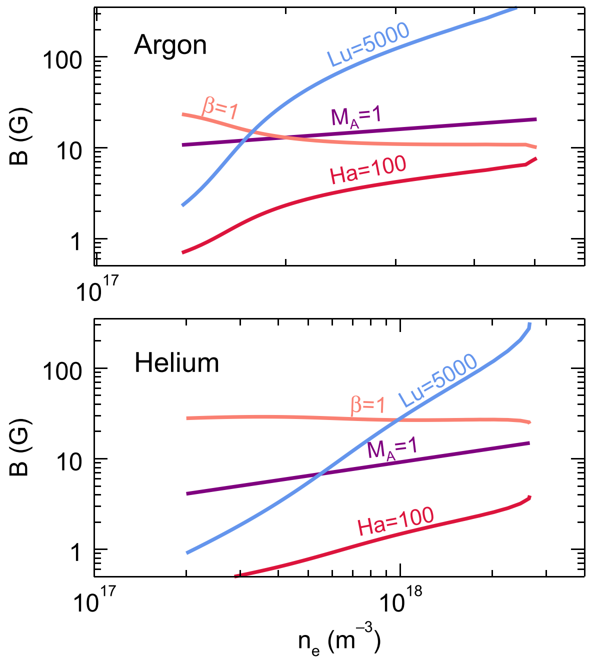

FIG. 12. The threshold magnetic field (G) for various astrophysically relevant dimensionless magnetic scaling parameters for (a) argon and (b) helium, the Alfvén Mach numbers $M_A = 1$, the Lundquist number $S = 5000$, and the Hartmann number $Ha = 100$. These values are predicted using the confinement code for a 300 kW discharge for $v_\phi = 10\,\mathrm{km/s}$ and $1\,\mathrm{G} < B < 100\,\mathrm{G}$.

Hartmann number is the ratio of the magnetic force to the viscous force $Ha = BL/\sqrt{\mu\eta} = \sqrt{ReRm}/M_A$ and is important in determining boundary layers. A Hartmann number $Ha = 100$ in MPDX is predicted for $B \sim 5\,\mathrm{G}$.

A. Dynamo scenarios

Kinematic dynamo simulations relevant to MPDX have been previously reported.[1,3–5] The process for experimental design is briefly reviewed to both emphasize the connection between the dimensionless parameters used in the modeling but also to illustrate how the experiments are planned to operate. The essence of the stirring is that the axisymmetric multi-cusp magnetic field and cathode stirring allow the azimuthal velocity profile (rotation) $v_\phi(\theta, t)$ to be controlled at the plasma boundary. Boundary driven flows are modeled by solving the incompressible Navier-Stokes equation

$$\frac{\partial \mathbf{v}}{\partial t} = \frac{1}{Re}\nabla^2\mathbf{v} - (\mathbf{v}\cdot\nabla)\mathbf{v} - \nabla p,\ \nabla\cdot\mathbf{v} = 0 \tag{7}$$

to determine the velocity field subject to the boundary condition $v_\phi(r = a, \theta, t) = f(\theta)$. Then, the solution to the Navier-Stokes is tested for dynamo behavior by finding the eigenmodes of the induction equation

$$\frac{\partial \mathbf{B}}{\partial t} = \frac{1}{Rm}\nabla^2\mathbf{B} + \nabla\times(\mathbf{v}\times\mathbf{B}),\ \nabla\cdot\mathbf{B} = 0, \tag{8}$$

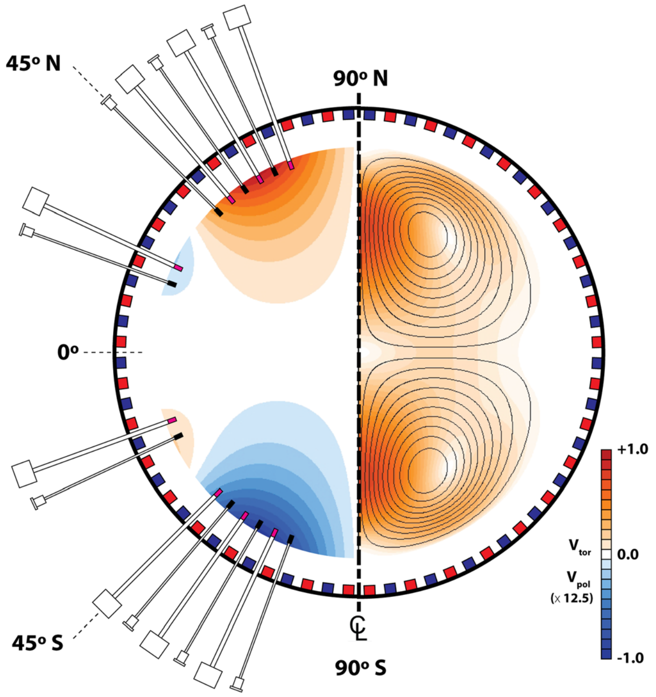

FIG. 13. Numerical simulations of the boundary driven flow for the flow drive with $Re = 300$ in a Von Kármán geometry with counter rotating flows in each hemisphere. The poloidal flows (right side) develop self-consistently as a response to the centrifugal forces developing due to toroidal (left) rotation.

which constitutes a kinematic dynamo problem.[3,4] Note the Lorentz force is not included in Eq. (7) when linear dynamo stability is being addressed. An example of a resulting velocity field is shown in Fig. 13 for one of the most promising scenarios for which the transition to a self-excited magnetic field is $Rm_{crit} \sim 300$.

Table I provides a list of experimental parameters for achieving slow dynamo action based on the simulations described above. The values of Re and Rm are from predictions of the dynamo growth rate in the simulations. These uniquely determine n_e and T_e for a given gas (μ), $T_i = 1\,\mathrm{eV}$ based on possible flow velocities v_ϕ. The dynamo problem is reduced to a confinement problem in MPDX and the power balance code is used to predict the input power and fill density required to achieve the desired plasma parameters. The equipartition dynamo field that satisfies $m_i n_i v_\phi^2/2 = B_{eqp}^2/2\mu_o$ is used as an approximation for the observable saturation magnetic field for dynamo action. The predicted magnetic fields are large enough to be measured by Hall probes, as is done in liquid metal dynamo experiments. The input power required is available, the edge rotation velocities have been measured in similar devices, and the equipartition field is large enough to be easily measured.

TABLE I. List of experimental parameters for achieving slow dynamos in MPDX.

Slow dynamo, $Re = 150$, $Rm = 300$		
Gas	Argon	Helium
n_e (m^{-3})	2×10^{17}	1.2×10^{18}
T_e (eV)	7.5	12
Power (kW)	100	140
v_ϕ (km/s)	6	3
B_{eqp} (G)	8	3

V. CONCLUSIONS

A new experiment for rotating unmagnetized plasma using $\mathbf{J} \times \mathbf{B}$ forcing in a magnetic bucket configuration has been described. The apparatus is suitable for new astrophysically relevant experiments on flow-driven plasma instabilities. As in previous magnetic buckets, the arrangement of permanent magnets into a multicusp configuration results in a large volume of uniform, unmagnetized plasma. A power balance calculation has shown that there is a large range of accessible Re, Rm, and Pm.

The MPDX continues to upgrade its power systems and diagnostics to approach parameters necessary for exciting dynamo action. Additional diagnostics to measure the ion distribution function and additional two-dimensional probe drives are planned for use.

ACKNOWLEDGMENTS

This work was funded in part by NSF Award No. PHY 0923258, ARRA MRI, NSF Award No. PHY 0821899, Center for Magnetic Self Organization in Laboratory and Astrophysical Plasmas, and DOE Award No. DE-SC0008709, Experimental Studies of Plasma Dynamos. C.C. acknowledges support by the ORISE Fusion Energy Sciences Graduate Fellowship.

[1] E. Spence, K. Reuter, and C. Forest, Astrophys. J. **700**, 470 (2009).
[2] M. Ossendrijver, Astron. Astrophys. Rev. **11**, 287 (2003).
[3] I. V. Khalzov, B. P. Brown, C. M. Cooper, D. B. Weisberg, and C. B. Forest, Phys. Plasmas **19**, 112106 (2012).
[4] I. V. Khalzov, B. P. Brown, E. J. Kaplan, N. Katz, C. Paz-Soldan, K. Rahbarnia, E. J. Spence, and C. B. Forest, Phys. Plasmas **19**, 104501 (2012).
[5] I. V. Khalzov, C. M. Cooper, and C. B. Forest, Phys. Rev. Let. **111**, 125001 (2013).
[6] S. A. Balbus and J. F. Hawley, Rev. Mod. Phys. **70**, 1 (1998).
[7] A. Gailitis, O. Lielausis, E. Platacis, G. Gerbeth, and F. Stefani, Rev. Mod. Phys. **74**, 973 (2002).
[8] K. Rahbarnia, B. P. Brown, M. M. Clark, E. J. Kaplan, M. D. Nornberg, A. M. Rasmus, N. Z. Taylor, C. B. Forest, F. Jenko, A. Limone, J.-F. Pinton, N. Plihon, and G. Verhille, Astrophys. J. **759**(2), 80 (2012).
[9] N. Katz, C. Collins, J. Wallace, M. Clark, D. Weisberg, J. Jara-Almonte, I. Reese, C. Wahl, and C. Forest, Rev. Sci. Instrum. **83**, 063502 (2012).
[10] C. Collins, N. Katz, J. Wallace, J. Jara-Almonte, I. Reese, E. Zweibel, and C. Forest, Phys. Rev. Lett. **108**, 115001 (2012).
[11] See http://www.solidworks.com for Solidworks.
[12] N. Hershkowtitz, K. Leung, and T. Romesser, Phys. Rev. Lett. **35**, 277 (1975).
[13] M. Ono, G. Greene, D. Darrow, C. B. Forest, H. Park, and T. Stix, Phys. Rev. Lett. **59**, 2165 (1987).
[14] L. Schmitz, R. Lehmer, G. Chevalier, G. Tynan, P. Chia, R. Doerner, and R. Conn, J. Nucl. Mater. **176–177**, 522 (1990).
[15] D. M. Goebel, R. M. Watkins, and K. K. Jameson, J. Propul. Power **23**, 3 (2007).
[16] C. M. Cooper, W. Gekelman, P. Pribyl, and Z. Lucky, Rev. Sci. Instrum. **81**, 083503 (2010).
[17] I. Hutchinson, *Principles of Plasma Diagnostics* (Cambridge, 2002).
[18] E. T. Everson, P. Pribyl, C. G. Constantin, A. Zylstra, D. Schaeffer, N. L. Kugland, and C. Niemann, Rev. Sci. Instrum. **80**, 113505 (2009).
[19] K. Leung, N. Hershkowtitz, and K. MacKenzie, Phys. Fluids **19**, 1045 (1976).
[20] D. G. Whyte, T. E. Evans, A. G. Kellman, D. A. Humphreys, A. W. Hyatt, T. C. Jernigan, R. L. Lee, S. L. Luckhardt, P. B. Parks, M. J. Schaffer *et al.*, in *Proceedings of the 24th European Conference on Controlled Fusion and Plasma Physics, Berchtesgaden, Germany* (1997), Vol. 21A, p. 1137.
[21] P. C. Stangeby, Phys. Fluids **27**, 682 (1984).